ACS NANO
Cite This: ACS Nano 2018, 12, 11481−11490
www.acsnano.org

ARTICLE

Formation of Si Hollow Structures as Promising Anode Materials through Reduction of Silica in $AlCl_3$−NaCl Molten Salt

Peibo Gao,[†] Xi Huang,[†] Yuting Zhao,[‡] Xudong Hu,[§] Dingcheng Cen,[†] Guohua Gao,[†] Zhihao Bao,*[,†] Yongfeng Mei,*[,‡] Zengfeng Di,*[,§] and Guangming Wu[†]

[†]Shanghai Key Laboratory of Special Artificial Microstructure Materials and Technology, School of Physics Science and Engineering, Tongji University, Shanghai 200092, China

[‡]Department of Materials Science, Fudan University, Shanghai 200433, China

[§]Shanghai Institute of Microsystem and Information Technology, Chinese Academy Science, Shanghai 200050, China

Supporting Information

ABSTRACT: **Hollow nanostructures are attractive for energy storage and conversion, drug delivery, and catalysis applications. Although these hollow nanostructures of compounds can be generated through the processes involving the well-established Kirkendall effect or ion exchange method, a similar process for the synthesis of the pure-substance one (*e.g.*, Si) remains elusive. Inspired by the above two methods, we introduce a continuous ultrathin carbon layer on the silica nano/microstructures (Stöber spheres, diatom frustules, sphere in sphere) as the stable reaction interface. With the layer as the diffusion mediator of the reactants, silica structures are successfully reduced into their porous silicon hollow counterparts with metal Al powder in $AlCl_3$−NaCl molten salt. The structures are composed of silicon nanocrystallites with sizes of 15−25 nm. The formation mechanism can be explained as an etching−reduction/nucleation−growth process. When used as the anode material, the silicon hollow structure from diatom frustules delivers specific capacities of 2179, 1988, 1798, 1505, 1240, and 974 mA h g^{-1} at 0.5, 1, 2, 4, 6, and 8 A g^{-1}, respectively. After being prelithiated, it retains 80% of the initial capacity after 1100 cycles at 8 A g^{-1}. This work provides a general way to synthesize versatile silicon hollow structures for high-performance lithium ion batteries due to the existence of ample silica reactants and can be extended to the synthesis of hollow structures of other materials.**

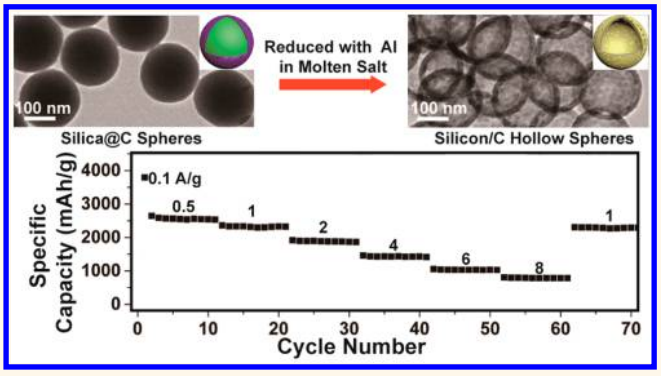

KEYWORDS: *silicon, hollow structures, anode, molten salt, carbon interface*

Hollow nanostructures (*e.g.*, shell, shell−core, nanotube, hollow polyhedral) have been intensively studied for applications, such as gas adsorption,[1] drug delivery,[2,3] energy storage and conversion,[4−11] and catalysis.[12−14] These hollow nanostructures of compounds can be formed through the self-templated processes such as the Kirkendall effect and ion exchange method.[15−21] The two processes spontaneously develop a continuous thin product layer at the initial stage of the reaction. Fan *et al.* have emphasized the importance of the layer in the formation of the hollow structure.[17] The layer can influence the outward and inward diffusion rates of mass and serve as the spatial confinement for the vacancies/voids to facilitate the formation of the hollow structure. For example, in the formation of hollow ZnO dandelions from Zn spheres, the spontaneously formed ZnO layer on the latter should be protected by ZnO_2^{2-} in the solution.[22] Otherwise, incomplete dandelions are formed. The above self-templated processes are rarely used to obtain the hollow structures of a pure substance, especially silicon, one of the most promising anode materials. Recently, the metals Mg and Al have been used to reduce various silica reactants into silicon-based nanomaterials.[23−25] Sandhage *et al.* have demonstrated the reduction of a biosilica template (diatom frustules) into shape-preserved porous silicon counterparts with gaseous Mg at 650 °C.[24] Very recently, in the molten salt system, these reactions are utilized to produce silicon nanoparticles at relatively low temperatures (200−500

Received: August 27, 2018
Accepted: November 1, 2018
Published: November 5, 2018

DOI: 10.1021/acsnano.8b06528
ACS Nano 2018, 12, 11481−11490

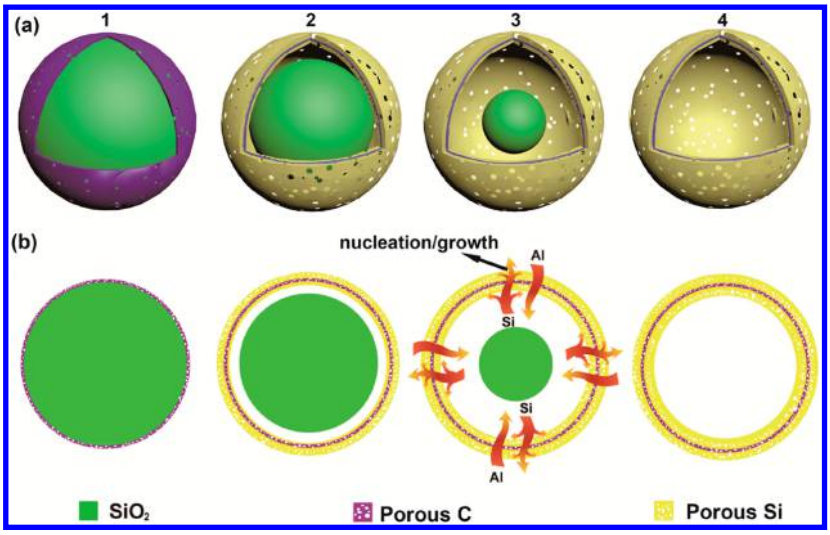

Figure 1. Schematic illustration of the formation of silicon hollow nanostructures through reduction of silica with Al powder in molten salts. In the formation process, the outward diffusion of Si/O elements is faster than the inward diffusion of Al element; then the cavity forms. The reduced Si nucleates and grows on the outer/inner surface of the carbon layer. Finally, a silicon hollow sphere forms.

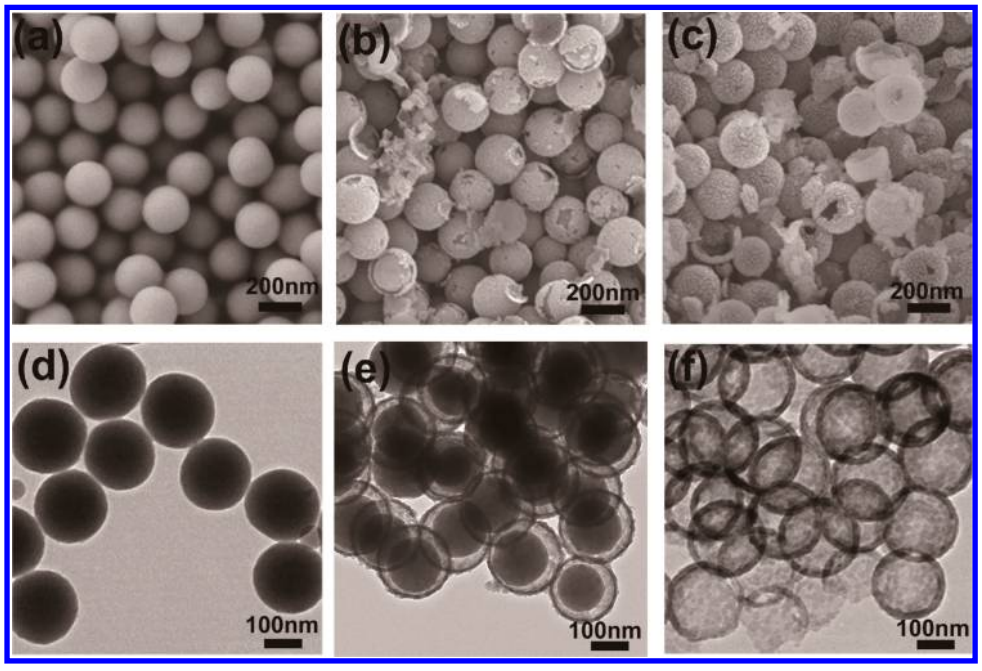

Figure 2. SEM and TEM images of the silicon hollow structure reduced with Al powder at different stages. (a, d) Raw carbon-coated silica spheres; (b, e) intermediate core/shell structure without enough Al reductant; (c, f) silicon hollow structure obtained from the reduction of the carbon-coated silica spheres together with subsequent acid etching.

°C).[26−28] However, the above processes fail to obtain hollow structures due to the absence of the stable interface in the reaction. Herein, we propose that such an interface can be constructed artificially prior to the reaction to tune the interdiffusion rates of reactants through the layer; then hollow structures can be formed. We demonstrate that micro/nanoscale silicon hollow structures are successfully synthesized from silica reactants (*e.g.*, Stöber spheres, diatom frustules, sphere in sphere) with a coated carbon layer as the initial layer in the reduction reaction in the molten salt at 300 °C. The synthesized silicon hollow structure from diatom frustules exhibits excellent rate performance with capacities of 2179, 1988, 1798, 1505, 1240, and 974 mA h g^{-1} at 0.5, 1, 2, 4, 6, and 8 A g^{-1}, respectively. After prelithiation, it retains 80% of the initial capacity after 1100 cycles at 8 A g^{-1}. This reported low-temperature reduction process can be extended to the synthesis of versatile silicon hollow structures from abundant silica-based raw materials for various applications.

RESULTS AND DISCUSSION

Formation and Characterization of Silicon Hollow Spheres. The formation process of silicon hollow sphere is illustrated in Figure 1. First, SiO_2 spheres are conformally coated with a continuous porous carbon layer to form carbon-coated SiO_2 spheres (Figure 1a1). The carbon layer works as a stable barrier interface in the reaction. In $AlCl_3$−NaCl molten salt, metal Al releases highly active electrons,[26,28,29] which attack the Si−O bond of the silica and liberate silicon. Since

DOI: 10.1021/acsnano.8b06528
ACS Nano 2018, 12, 11481−11490

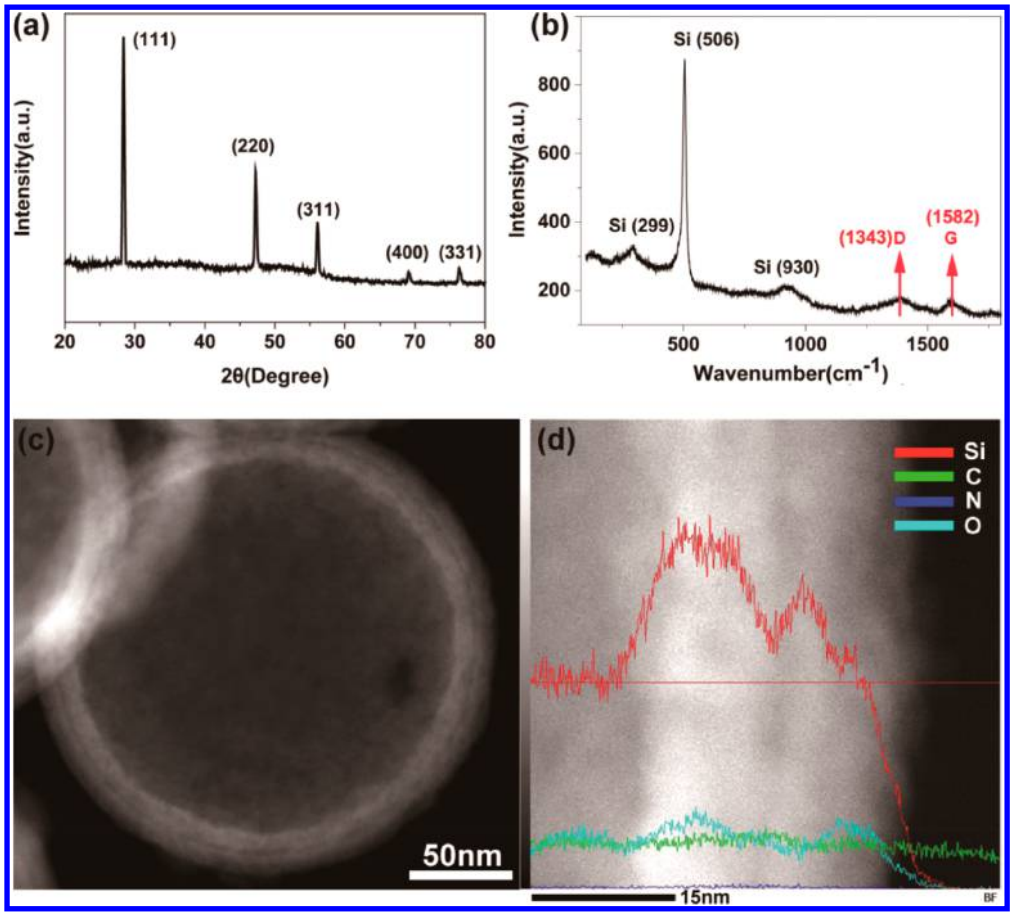

Figure 3. (a) XRD patterns, (b) Raman spectrum, (c) Cs-corrected TEM image, and (d) EDS profile of the obtained silicon hollow spheres.

the diffusion of silicon and oxygen is outward and faster than inward diffusion of the reducing reactant (*e.g.*, subvalent Al) due to the existence of the carbon layer, then voids/cavities can be formed. While silica is reduced by Al, silicon nucleates and grows on the carbon shell and the core/shell nanostructure (Figure 1a2) is produced. As the reaction proceeds, the shell of the structure (Figure 1a3) becomes thick while SiO_2 is further consumed. At the end of the reaction, a hollow sphere (Figure 1a4) can be generated. On the contrary, due to the volume change upon the reduction of uncoated silica, the formed silicon particles shatter and finally evolve into nearly spherical Si nanoparticles to minimize the overall surface energy,[28] as shown in Figure S1. In this study, highly uniform silica spheres (Figure 2a) with a diameter of 206.5 ± 2.4 nm are synthesized through the traditional Stöber method.[30] Then, polydopamine (pDA) is coated on the silica spheres. After the carbonization process, the desired carbon layer (~2.2 nm), which will act as a diffusion barrier, is formed conformally on the silica spheres, as observed by transmission electron microscopy (TEM) imaging (Figure S2). The carbon-coated silica spheres are reduced with Al powder in $AlCl_3$−NaCl molten salt at 300 °C for 12 h. The mixture of $AlCl_3$−NaCl with the molar ratio of 3:2 is used here to lower the pressure of $AlCl_3$ for easy handling. According to the phase diagram (Figure S3) of the $AlCl_3$−NaCl binary system, the mixture is liquid at 300 °C, while pure $AlCl_3$ is in liquid−gas phase. This is consistent with a larger weight loss of $AlCl_3$ compared with the salt mixture in the evaporation experiment (Figure S4). The scanning electron microscopy (SEM) image (Figure 2b) and TEM image (Figure 2e) show the morphology of the semifinished product after the partial reaction and subsequent acid etching. The partially reacted product has a the core/shell structure. The core is believed to be the unreacted silica. When further reacted with enough Al reductant to allow the reaction to complete, the solid Stöber spheres turn into hollow spheres, as revealed by SEM (Figure 2c) and TEM (Figure 2f) images. To exclude the possibility that the cavity in the hollow sphere is formed by HF acid etching, ethanol is used as the only solvent to remove the salt. As indicated in the TEM image (Figure S5), the cavity remains after ethanol washing, indicating the hollow structure is formed by the reaction prior to the etching process. The shell of the hollow sphere is porous with a thickness of ~20 nm, as shown in its TEM image (Figure S6). The phase transformation during the reaction is further revealed by X-ray diffraction (XRD) analyses. The pattern (Figure S7) of the crude product after reduction indicates the formation of $NaAlCl_4$ and AlOCl. The diffraction peaks of $AlCl_3$ are from the excess reagents in the system. The characteristic diffraction peak of Si (at ~28.5°) can still be observed, although a large amount of salt and byproduct is involved in the system. The above results suggest that the reaction in $AlCl_3$−NaCl molten salt may run as follows:

$$4Al + 3SiO_2 + 3AlCl_3 + NaCl \rightarrow 3Si + 6AlOCl + NaAlCl_4 \quad (1)$$

After HCl and HF washing, the byproducts are easily removed, as confirmed by XRD patterns (Figure 3a). According to Sherrer's equation, the average size of the silicon crystallite is calculated to be ~23 nm. The Raman spectrum of

DOI: 10.1021/acsnano.8b06528
ACS Nano 2018, 12, 11481−11490

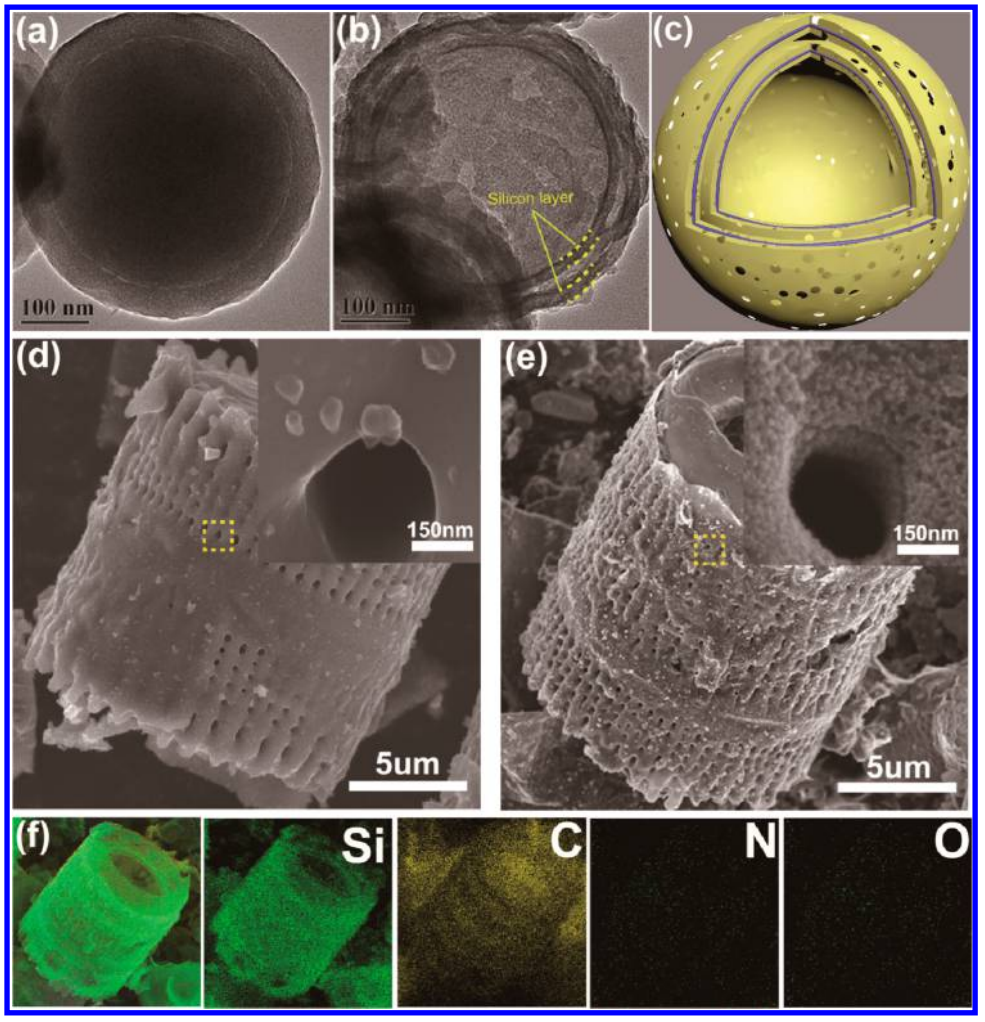

Figure 4. TEM images of SiO_2@C@SiO_2@C before (a) and after (b) reduction; (c) schematic illustration of the final product; SEM images of diatom frustules before (d) and after (e) reduction (insets of d and e are the enlarged SEM images of the squared area); (f) STEM and related element mapping of the converted diatom frustules.

the product (Figure 3b) shows a characteristic peak of silicon at around 506 cm^{-1} together with broad peaks located at around 299 and 930 cm^{-1}, corresponding to the overtones of TA(X) and TO(L) modes, respectively.[31,32] The Raman peak shifts toward a lower wavenumber compared to that of crystalline Si (521 cm^{-1}),[33,34] indicating that the as-prepared Si hollow sphere has a small crystalline size together with an amorphous silicon phase.[34−37] In addition, the D and G bands appear at 1343 and 1582 cm^{-1}, respectively, confirming the existence of carbon, which originates from the carbon barrier layer in the product.[35,38] The silicon nature of the shell is further confirmed by high-resolution TEM analyses (Figure S8). The spacing of the lattice fringe is measured to be 0.31 nm, which corresponds to the (111) plane of the silicon fcc phase.[33] Figure 3c shows the spherical aberration corrected TEM (Cs-corrected TEM) image of the product. It is observed that the overall shell is split into two parts by a middle carbon barrier layer. Energy-dispersive X-ray spectroscopy (EDS) analysis of the shell is shown in Figure 3d. Only the silicon signal is predominant in the shell layer. The low intensity of carbon element indicates that the pDA-derived carbon layer may be covered by silicon. In the middle of the shell, the decrease of silicon signal intensity and slight increase of carbon intensity are due to the appearance of the carbon layer, which indicates that the shell is formed by a Si/C/Si sandwiched layer.

Formation and Characterization of Other Silicon Structures. The process also works on the more complex silica structures to synthesize corresponding silicon hollow structures. For example, the spheres with multiple layers of C/SiO_2 (SiO_2@C@SiO_2@C) are synthesized *via* the combination of Stöber and sol−gel methods.[39] The TEM image (Figure 4a) of the structure shows an obvious bonding between the two layers. After the same reduction process, a sphere in sphere structure, or the so-called matryoshka structure, can be clearly observed in the SEM (Figure S9) and TEM images (Figure 4b) of the product. The details of the structure are illustrated in Figure 4c. Each shell consists of the intermediate carbon layer and the two sides of silicon layers. Besides the nanoscale object, the process can work on the very intricate 3D silica microscale structures, diatom frustules. SEM images (Figure 4d and e) show the morphology of the *Aulacoseira* frustules before and after reduction. In contrast to the smooth surface (Figure 4d, inset) of the diatom frustules, the synthesized silicon hollow structure exhibits a rougher surface after the reaction. STEM images (Figure 4f) show its related element mapping of the converted diatom frustules. Among them, the carbon and nitrogen signals inherited from

DOI: 10.1021/acsnano.8b06528
ACS Nano 2018, 12, 11481−11490

pDA appear uniformly throughout the product, indicating that a conformal carbon layer exists in it. HRTEM and nitrogen adsorption−desorption analyses (Figure S10) are conducted to provide detailed structural information on the silicon hollow structure from diatom frustules. The structure is porous and consists of a large amount of aggregated nanoparticles with a size range from 15 to 25 nm, which is in good agreement with the XRD result (Figure S11). The X-ray microscopy image (Figure S12) is further used to reveal the interior structure of the converted diatom frustule. A 2D section image of the converted diatom frustules confirms its hollow walls, while it is solid in the unconverted diatom frustules.

Formation Mechanism of Silicon Hollow Structures. To further study the reaction mechanism, the morphology evolution with the reaction is studied by examining the product after different reaction times and subsequent etching. TEM images (Figure S13b and c) show the morphologies of the products reacted for 3 and 6 h, respectively. They exhibit a core/shell structure due to the incomplete reaction. Based on the images, the size histograms of outside diameters (o.d.s) and inside diameters (i.d.s) of the product are shown in Figure S14 and Figure S15, respectively. The calculated results are summarized in Table 1. After 3, 6, and 12 h of reaction, o.d.s are 211.3 ± 2.6, 214.0 ± 2.7, and 216.2 ± 3.0 nm, while i.d.s are 204.8 ± 1.3, 204.2 ± 1.7, and 196.6 ± 1.3 nm, respectively. After the reaction, o.d.s and i.d.s of the shell lie on both sides of the initial size (206.5 ± 2.4 nm) of the silica spheres. In the early stage of reaction, o.d. increases dramatically, while i.d. decreases mainly at the late reaction stage. The results reveal that in the early stage outward diffusion of Si through the carbon layer is predominant. To manifest the function of the pDA-derived carbon layer in the mass transfer, the product after the reaction without acid etching is examined. The TEM image (Figure S16) without obvious contrast indicates the solid nature of the product. We believe that the molten salt enters the cavity due to the porous structure of the pDA-derived carbon layer and the formed silicon product layer.[40] The porous product layer may be developed in the following process. The silicon nucleates on sites of the porous carbon layer. As the reaction proceeds, silicon particles growing at neighboring sites encounter each other and form the pores. After the salt or AlOCl trapped in them is removed, the porous structure is formed. For comparison, using atomic layer deposition (ALD), the Stöber sphere is also coated by a thin layer of Al_2O_3 without pinholes. The TEM image (Figure S17) without the contrast difference confirms the homogeneous structure of the product after the reaction and subsequent acid etching. Thus, the shell structure cannot be formed if mass transfers through the solid layer. The following mechanism may account for the experiment result. First, the formation of subvalent aluminum follows the reversible reaction below:[41]

$$3Al(I) \leftrightarrow 2Al(0) + Al(III) \quad (2)$$

The continuous porous pDA-derived carbon layer mainly limits the inward diffusion of Al(I). It can be in the form of AlCl, which etches SiO_2 to break the Si−O bond to form SiO_x.

Table 1. Outside Diameters (o.d.s) and Inside Diameters (i.d.s) of the Formed Silicon Shell after Different Reaction Times

	reaction time (h)			
	0	3	6	12
o.d. (nm)	206.5 ± 2.4	211.3 ± 2.6	214.0 ± 2.7	216.2 ± 3.0
i.d. (nm)		204.8 ± 1.3	204.2 ± 1.7	196.6 ± 1.3

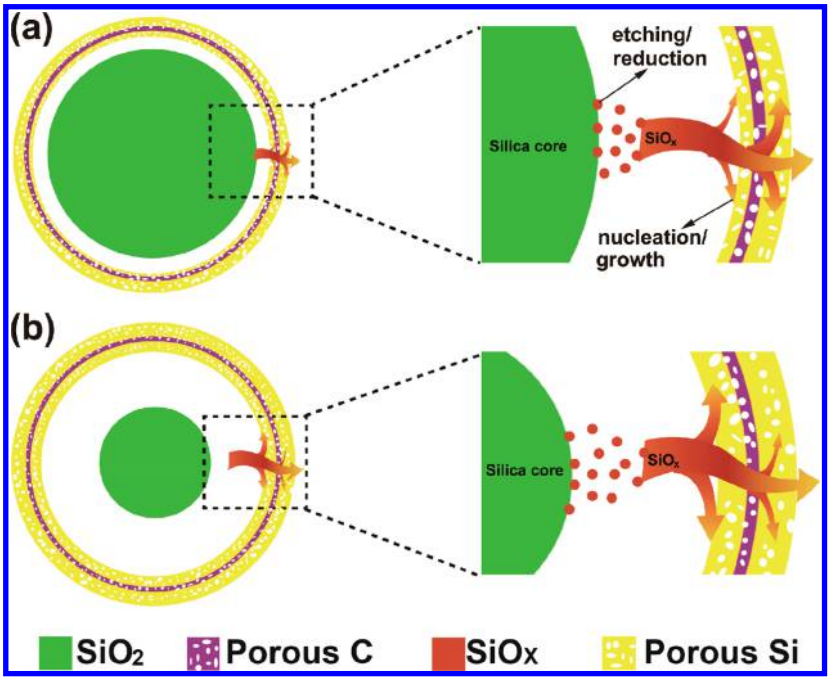

Figure 5. Schematic illustration of the silicon hollow structure formation by a diffusion mechanism in the molten salt. (a) At the early stage, more partially reduced SiO_x diffuses through the porous carbon layer, and the reduced Si nucleates and grows on the outer surface; (b) in the late stage, SiO_x takes more time to diffuse to the carbon layer due to the shrinkage of silica core, or the formed product layer blocks the outward diffusion of SiO_x more than the inward diffusin of Al(I). More Si can be reduced and grow near/on the inner surface of the product layer.

DOI: 10.1021/acsnano.8b06528
ACS Nano 2018, 12, 11481−11490

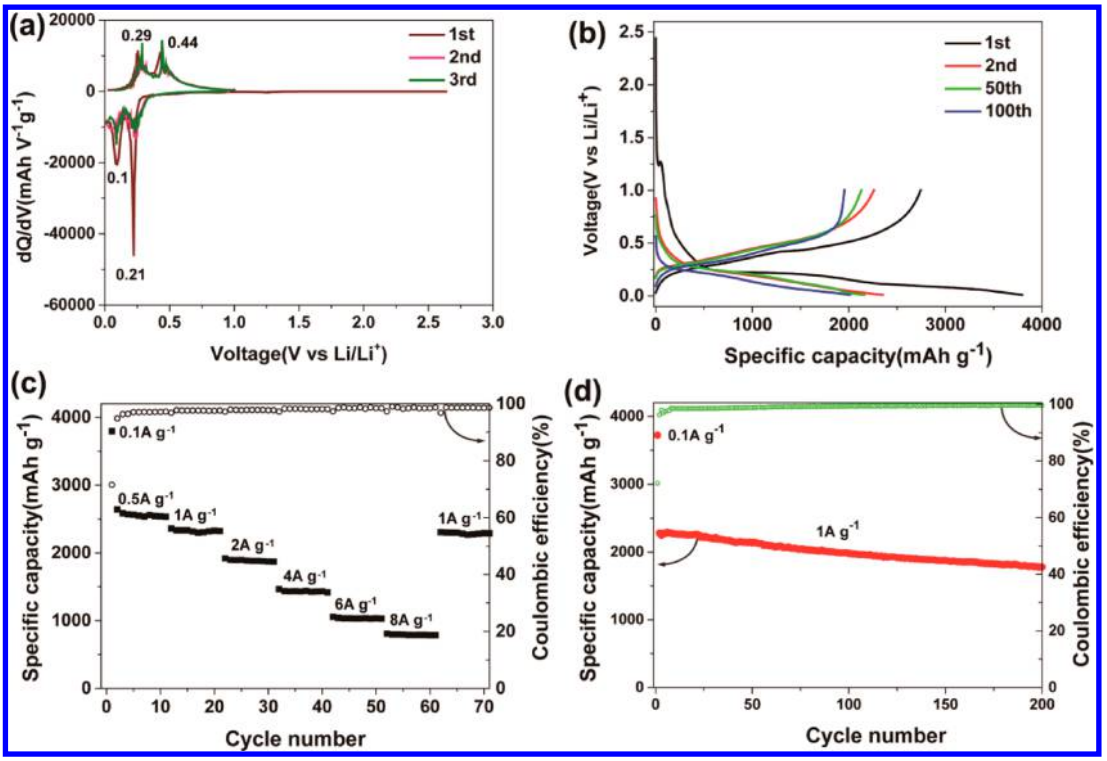

Figure 6. (a) Plots of the differential capacity *versus* voltage, (b) the discharge/charge curve at 0.1 A g^{-1} for the initial cycle and 1 A g^{-1} for the subsequent cycle, and (c) rate and (d) cycling performance of the silicon hollow spheres.

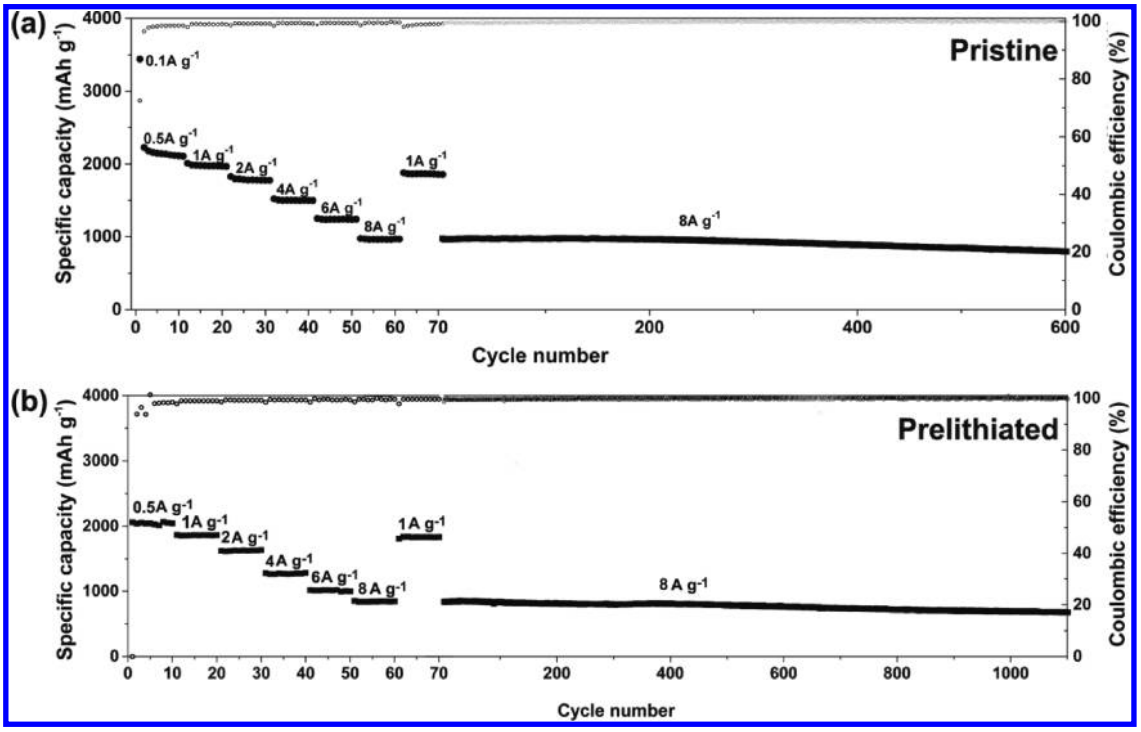

Figure 7. Rate and cycling performance of pristine (a) and prelithiated (b) anodes based on a hollow silicon structure reduced from diatom frustules.

This is confirmed by the smooth surface of the unreacted silica core shown in Figure 2e. Due to low concentration of Al(I) at the SiO_2 interface, it cannot fully reduce SiO_x into Si. Since the diffusion of subvalent Al through the carbon shell is slow and becomes the limiting step at the early stage of the reaction. More SiO_x diffuses through the porous carbon layer and enters the higher concentrated Al(I) region and is fully reduced into the Si. It then nucleates and grows on the outer surface of the carbon layer (Figure 5a). In the late stage, SiO_2 cores shrink a lot. The partially reduced SiO_x takes more time to diffuse to the carbon shell or the product layer. Or the formed product layer somehow blocks the outward diffusion of SiO_x more than

DOI: 10.1021/acsnano.8b06528
ACS Nano 2018, 12, 11481−11490

the inward diffusion of Al(I). It may allow more Al(I) species to have enough time to penetrate through the product/carbon layer and enter the cavity. Then more silicon can be fully reduced near/on the inner surface of the product layer (Figure 1b and Figure 5b). Finally, the silicon layer mainly grows inward. In all, the whole process can be summarized as an etching−reduction/nucleation−growth process.

Electrochemical Performance of Si Hollow Structures. Since the silicon hollow structures have been regarded as one of the most fascinating anode materials for lithium ion battery (LIB) applications, the electrochemical performances of our synthesized structures are evaluated. Figure 6a shows the differential capacity *versus* voltage profiles of the electrode of silicon hollow spheres. During the first discharge process, there are peaks at ∼0.21 and ∼0.1 V, corresponding to the lithiation process of amorphous Si and crystallized Si, respectively.[42] We speculate the appearance of the amorphous silicon is due to low synthesis temperature, which is confirmed by our previous reports.[35] Figure 6b shows the discharge/charge curves of the electrode of silicon hollow spheres at various cycle numbers. The initial discharge capacity is 3795.3 mA h g^{-1}, while the initial Coulombic efficiency (CE) is only 72.3%. After only three cycles, the CE of the electrode increases up to 98.4%. The amorphous Si phase may slightly lower the first CE, and conversely it is advantageous to improve the long-term cycling life.[43,44] As shown in Figure 6c, the reversible capacities of the Si anode are 2534, 2324, 1868, 1416, 1029, and 785 mA h g^{-1} at 0.5, 1, 2, 4, 6, and 8 A g^{-1}, respectively. Importantly, when the current density returns to 1 A g^{-1} after cycling at the high rates, a high capacity of 2291 mA h g^{-1} is still preserved. The cycling stability of the electrode of silicon hollow spheres is shown in Figure 6d. After 200 cycles, the electrode delivers a reversible capacity as high as 1774 mAh g^{-1} at 1 A g^{-1}, which corresponds to 79.8% retention. The stable capacity reveals that the presence of the carbon layer is able to maintain the structural integrity of the silicon hollow sphere during the discharge/charge process. Figure S18 shows the morphology of the silicon hollow sphere after 100 cycles at 1 A g^{-1}; the spherical shape is still retained. The electrochemical performance is even better for the electrode of the silicon hollow structure from diatom frustules. As shown in Figure 7a, the reversible capacities of the silicon hollow structure anode are 2179, 1988, 1798, 1505, 1240, and 974 mA h g^{-1} at 0.5, 1, 2, 4, 6, and 8 A g^{-1}, respectively. The electrode of the silicon hollow structure undergoes negligible capacity fading after 600 cycles at a high rate of 8 A g^{-1}, showing a reversible capacity of 797 mA h g^{-1} with a retention of 81.7%. For the conventional Si nanoparticles without a hollow structure, the rate and long-term cycling capacities are not satisfactory (Figure S19). The good performance of the capacity retention is also well consistent with the impedance analyses. The resulting Nyquist plots (Figure S20) of the electrodes of the silicon hollow structure display a normal impedance behavior in the high to medium frequency region, which is associated with the charge transfer.[45] The impedance variance of the electrode of the silicon hollow structure is negligible between the 100th and 200th cycles, which indicates a more stable interphase formed on the carbon shell of the silicon hollow composite.[46] Furthermore, the electrode of the silicon hollow structure shows a better rate performance and long-term cycling stability at high rates than porous Si in previously reported works (Figure S21). For its potential practical application, a prelithiated electrode of a silicon hollow structure is obtained by a simple self-discharge mechanism (Figure S22).[46,47] Remarkably, the lithiated electrode exhibits significantly enhanced performance by increasing the initial CE to 93.6% compared to 75.6% of a pristine electrode. After lithiation, the long-term life can be extended to 1100 cycles with 80% retention at 8 A g^{-1} (Figure 7b).

Although our etching−reduction/nucleation−growth process produces a similar hollow structure to the process of the Kirkendall effect, there is some difference. In the latter one, for the successful formation of hollow structures, the initial layer at the early stage of the reaction will be developed. This layer prevents a direct penetration or evaporation of the reactant and hence establishes a solid diffusion medium. It does not allow the reactant to enter the cavity, which is formed through the void merging. However, the carbon layer introduced in our process is porous, and thus it allows the reactant with a liquid medium to enter into the cavity of the product. The formation of the cavity is mainly due to the etching effect of subvalent Al on SiO_2. The carbon layer also contributes to the superior electrochemical performance of the silicon hollow structure. Since the sandwiched shell is porous, the electrolyte can penetrate the carbon layer and react with it to form a stable solid-electrolyte interphase (SEI) in the following discharge/charge process. It can protect the inner silicon layer. Thus, it partially improves the stability of the electrode. However, the outer silicon layer directly contacting the electrolyte has no such protection. An additional carbon layer can be coated on the entire hollow silicon structure to form a double-carbon-coated sphere, further improving its electrochemical performance. Meanwhile, it improves the electrical conductivity to enhance the rate performance.[5,48] The carbon layer also provides mechanical clamping so that the volume mainly expands inward.[49] SEM images (Figure S23) of the cross-section of the electrode before and after the lithiation show that the thickness has a negligible increase. The internal cavity of the silicon hollow structure and porous shell can effectively accommodate the volume change during the electrochemical reaction and prevent the cracking of the active Si material. Thus, it maintains the electrical contact and structural integrity of the electrode and finally increases the long-term stability of the electrode.

CONCLUSIONS

In summary, a silicon hollow sphere is prepared by reduction of a carbon-coated silica sphere at 300 °C with metal Al powder in a molten salt. The coated carbon layer can adjust the interdiffusion of the reactants, influence the mass transfer at the interface, and facilitate the formation of the hollow structure. The method is also applicable to more complicated silica templates (*e.g.*, diatom frustules, sphere in sphere) to synthesize the silicon hollow structure. As anode materials, the obtained silicon hollow structures exhibit high capacity, long cycling, and excellent rate performance. The silicon hollow sphere delivers specific capacities of 1774 mA h g^{-1} after 200 cycles at a current density of 1 A g^{-1}, while the silicon hollow structure from diatom frustules delivers stable capacities of 797 mA h g^{-1} after 600 cycles at 8 A g^{-1}. After the prelithiation process, it retains 80% of the initial capacity after 1100 cycles at 8 A g^{-1}. With the creation of an artificial layer to adjust the interdiffusion of the starting reactants, this reported process can be extended to the synthesis of versatile silicon hollow structures from abundant silica-based raw materials for various applications.

DOI: 10.1021/acsnano.8b06528
ACS Nano 2018, 12, 11481−11490

EXPERIMENTAL SECTION

Preparation of the Silica Spheres. The monodisperse SiO_2 spheres were prepared with the Stöber method.[30] Specifically, TEOS ($Si(OC_2H_5)_4$, 1.30 mL, 99 wt %, AR) and 45.50 mL of absolute ethanol were mixed to form a solution, while water (1.80 mL), NH_4OH (1.35 mL, 28 wt %, AR), and absolute ethanol (46.85 mL) formed another solution. Then the above two solutions were mixed rapidly and stirred at room temperature for 0.5 h (or 2 h) to form a white colloidal suspension. The silica particles with different diameters were obtained by centrifuging the suspension and washing the precipitate with ethanol three times.

Preparation of the SiO_2@C and SiO_2@C@SiO_2@C Spheres. The obtained SiO_2 spheres (stirred for 0.5 h) were dispersed in 50 mL of Tris-buffer solution (10 mM, PH 8.5). Then, 100 mg of dopamine was added under stirring for 5 h to coat the SiO_2 spheres with a pDA layer. Next, the SiO_2@pDA spheres were collected by filtration, washed with DI water, and dried at 60 °C for 2 h. To prepare the multiple-layered SiO_2/C spheres, first, the SiO_2 spheres (stirred for 2 h) were coated with a pDA layer. Then, the dried powder was redispersed in a mixture of 80 mL of ethanol, 19 mL of water, and 1 mL of concentrated ammonium hydroxide by stirring. Then, 1 mL of TEOS was added dropwise into the above solution and stirred for 12 h. SiO_2@pDA@SiO_2 nanoparticles were collected by centrifugation and washed using ethanol. Third, the second pDA layer was coated onto the SiO_2@pDA@SiO_2 powders. Finally, the pDA layer was carbonized at 800 °C for 2 h under an Ar atmosphere.

Preparation of Carbon-Coated Diatom Frustules. The commercially available diatom frustules (1.0 g, Alfa Aesar) were well dispersed in 200 mL of Tris-buffer solution (10 mM, pH 8.5). Then, 400 mg of dopamine was added under stirring for 5 h to coat the diatom frustules with a pDA layer. Next, the coated diatom frustules were collected by filtration and washed with 200 mL of DI water. The dried powder was carbonized at 800 °C in an Ar atmosphere for 2 h in a tube furnace with a heating rate of 5 °C min^{-1} to obtain the carbon-coated diatom frustules.

Preparation of the SiO_2@ Al_2O_3 by ALD Deposition. The SiO_2 spheres were coated with Al_2O_3 by an atomic layer deposition process with a Picsun SUNALE R-100 atomic layer deposition system. During the deposition, the chamber was maintained at 1 mbar with N_2 gas at 200 sccm. Al_2O_3 was deposited at 200 °C with trimethylaluminum (TMA) and H_2O precursors, and 30 cycles were used to deposit about 2.5 nm thick Al_2O_3. After the reaction, the obtained powders were dried at 80 °C.

Preparation of Si Hollow Structures. The obtained SiO_2/C composites (1 g) were mixed with Al powder (0.85 g), $AlCl_3$ (4 g), and NaCl (1.16 g) thoroughly. The mixture was loaded in a stainless steel autoclave and sealed in a glovebox filled with Ar. Thereafter, it was heated to 300 °C at a ramping rate of 5 °C min^{-1} and kept at this temperature overnight in a H_2 (5 vol %)/Ar (95 vol %) flow. After cooling to room temperature within a furnace, the obtained powder was stirred in 3 M HCl solution for 6 h to remove Al-bearing and excessive salt. To remove the residual SiO_2, the powder was immersed in ethanol-based hydrofluoric acid (HF, 5%) solution for 5 min followed by washing with ethanol and then vacuum-dried at 60 °C for 3 h.

Characterization of Materials. The morphologies of samples were characterized by field-emission scanning electron microscopy (FESEM) with an Ultra 55 operating at 10 keV. XRD patterns were performed on a Rigaku D/Max-RB diffractometer with Cu Kα radiation. TEM analyses were operated on a JEOL JEM-2010 electron microscope operated at 200 keV. Cs-corrected TEM was conducted with a JEM-ARM300F. The energy dispersive spectroscopy of Si@C was recorded with an Oxford Instruments X-MAX 50. The nitrogen adsorption and desorption isotherms were obtained using the Brunauer–Emmett–Teller method at 77 K after degassing the sample at 200 °C for 4 h by a Micrometrics ASAP 2010 analyzer. Raman spectra were obtained from a Renishaw Raman spectrometer with a 632.8 nm excitation laser. The X-ray microscopy image was obtained with an Xradia 810 Ultra.

Electrochemical Properties of the Anode of Si Hollow Structures. For preparing the electrode, Si hollow structure as the active materials, super P carbon black, and sodium alginate as the binder in a weight ratio of 6:2:2 in DI water were mixed and formed a slurry. The slurry was then pasted on Cu foil and dried at 75 °C under vacuum for 12 h. The cast electrodes were punched into disks with a diameter of 12 mm, and the active mass was determined to be about 0.5–0.7 mg cm^{-2}. CR2016 cells were assembled in an argon-filled glovebox for the testing of electrochemical properties. In the test, pure Li foils were used as the counter electrode and the electrolyte was a 1.0 M $LiPF_6$ solution in a mixed solvent of ethylene carbonate and diethyl carbonate (DoDoChem, China, 1:1 (v/v)) with 10 wt % fluoroethylene carbonate as the additive. The galvanostatic discharge/charge performance was conducted between 0.01 and 1.0 V on an automatic battery testing system (LAND CT2001A) at 25 °C. Electrochemical impedance spectroscopy was recorded from 100 kHz to 0.01 Hz with an electrochemical workstation (AutoLab 302N), and the amplitude was 10 mV. The specific capacity of the electrode was calculated according to the total weight of Si/C composites.

Prelithiation of the Electrode of Si Hollow Structures. An electrode of a Si hollow structure was directly contacted with a piece of lithium foil in the presence of electrolyte between them. An external press was applied to them using a stainless steel plate. The Si/Li alloying reaction could occur spontaneously when the electrode of the hollow C/Si structure and Li foil were short.

ASSOCIATED CONTENT

Supporting Information

The Supporting Information is available free of charge on the ACS Publications website at DOI: 10.1021/acsnano.8b06528.

Additional information (PDF)

AUTHOR INFORMATION

Corresponding Authors

*E-mail: zbao@tongji.edu.cn.
*E-mail: yfm@fudan.edu.cn.
*E-mail: zfdi@mail.sim.ac.cn.

ORCID

Zhihao Bao: 0000-0002-8708-7510
Yongfeng Mei: 0000-0002-3314-6108
Zengfeng Di: 0000-0002-9357-5107

Author Contributions

Z.B., G.G., Y.M., Z.D., and G.W. conceived the idea and planned the details of the experiment. P.G., X.H., X.H., Y.Z., and D.C. carried out the materials synthesis and characterization. All authors cowrote the manuscript.

Notes

The authors declare no competing financial interest.

ACKNOWLEDGMENTS

This work was supported by the National Science Foundation of China programs (Nos. U1503292, U1703128, and 212711400), the Program of Shanghai Academic/Technology Research Leader (16XD1404200), Key Research Project of Frontier Science, Chinese Academy of Sciences (QYZDBSSW-JSC021), the Fundamental Research Funds for the Central Universities (22120180231), and National Science and Technology Major Project (2016ZX02301003). We thank Dr. Youli Hong and Mr. Xiaochun Qian, from Carl Zeiss (Shanghai) Co., LTD, for collection and analysis of data on X-ray microscopy images.

DOI: 10.1021/acsnano.8b06528
ACS Nano 2018, 12, 11481–11490

REFERENCES

(1) Hu, J.; Cai, H.; Ren, H.; Wei, Y.; Xu, Z.; Liu, H.; Hu, Y. Mixed-Matrix Membrane Hollow Fibers of $Cu_3(BTC)_2$ MOF and Polyimide for Gas Separation and Adsorption. *Ind. Eng. Chem. Res.* **2010**, *49*, 12605−12612.

(2) Li, Y. Y.; Cunin, F.; Link, J. R.; Gao, T.; Betts, R. E.; Reiver, S. H.; Chin, V.; Bhatia, S. N.; Sailor, M. J. Polymer Replicas of Photonic Porous Silicon for Sensing and Drug Delivery Applications. *Science* **2003**, *299*, 2045−2047.

(3) Cao, S.; Fang, L.; Zhao, Z.; Ge, Y.; Piletsky, S.; Turner, A. P. F. Hierachically Structured Hollow Silica Spheres for High Efficiency Immobilization of Enzymes. *Adv. Funct. Mater.* **2013**, *23*, 2162−2167.

(4) Huang, X.; Yang, J.; Mao, S.; Chang, J.; Hallac, P. B.; Fell, C. R.; Metz, B.; Jiang, J.; Hurley, P. T.; Chen, J. Controllable Synthesis of Hollow Si Anode for Long-Cycle-Life Lithium-Ion Batteries. *Adv. Mater.* **2014**, *26*, 4326−4332.

(5) Sim, S.; Oh, P.; Park, S.; Cho, J. Critical Thickness of SiO_2 Coating Layer on Core@Shell Bulk@Nanowire Si Anode Materials for Li-Ion Batteries. *Adv. Mater.* **2013**, *25*, 4498−4503.

(6) Liu, N.; Wu, H.; McDowell, M. T.; Yao, Y.; Wang, C. M.; Cui, Y. a Yolk-Shell Design for Stabilized and Scalable Li-Ion Battery Alloy Anodes. *Nano Lett.* **2012**, *12*, 3315−3321.

(7) Chen, S.; Shen, L.; van Aken, P. A.; Maier, J.; Yu, Y. Dual-Functionalized Double Carbon Shells Coated Silicon Nanoparticles for High Performance Lithium-Ion Batteries. *Adv. Mater.* **2017**, *29*, 1605650.

(8) Song, T.; Xia, J.; Lee, J. H.; Lee, D. H.; Kwon, M. S.; Choi, J. M.; Wu, J.; Doo, S. K.; Chang, H.; Park, W. I.; Zang, D. S.; Kim, H.; Huang, Y.; Hwang, K. C.; Rogers, J. A.; Paik, U. Arrays of Sealed Silicon Nanotubes as Anodes for Lithium Ion Batteries. *Nano Lett.* **2010**, *10*, 1710−1716.

(9) Wu, H.; Chan, G.; Choi, J. W.; Ryu, I.; Yao, Y.; McDowell, M. T.; Lee, S. W.; Jackson, A.; Yang, Y.; Hu, L.; Cui, Y. Stable Cycling of Double-Walled Silicon Nanotube Battery Anodes through Solid-Electrolyte Interphase Control. *Nat. Nanotechnol.* **2012**, *7*, 310−315.

(10) Lin, H.; Weng, W.; Ren, J.; Qiu, L.; Zhang, Z.; Chen, P.; Chen, X.; Deng, J.; Wang, Y.; Peng, H. Twisted Aligned Carbon Nanotube/Silicon Composite Fiber Anode for Flexible Wire-Shaped Lithium-Ion Battery. *Adv. Mater.* **2014**, *26*, 1217−1222.

(11) Zhang, J.; Hu, H.; Li, Z.; Lou, X. W. Double-Shelled Nanocages with Cobalt Hydroxide Inner Shell and Layered Double Hydroxides Outer Shell as High-Efficiency Polysulfide Mediator for Lithium-Sulfur Batteries. *Angew. Chem., Int. Ed.* **2016**, *55*, 3982−3986.

(12) He, Y.; Sui, F.; Kauzlarich, S. M.; Galli, G. Si-Based Earth Abundant Clathrates for Solar Energy Conversion. *Energy Environ. Sci.* **2014**, *7*, 2598−2602.

(13) Wang, L.; Peng, B.; Guo, X.; Ding, W.; Chen, Y. Ferric Molybdate Nanotubes Synthesized based on the Kirkendall Effect and Their Catalytic Property for Propene Epoxidation by Air. *Chem. Commun.* **2009**, 1565−1567.

(14) Wang, J. X.; Ma, C.; Choi, Y.; Su, D.; Zhu, Y.; Liu, P.; Si, R.; Vukmirovic, M. B.; Zhang, Y.; Adzic, R. R. Kirkendall Effect and Lattice Contraction in Nanocatalysts: a New Strategy to Enhance Sustainable Activity. *J. Am. Chem. Soc.* **2011**, *133*, 13551−13557.

(15) Yin, Y.; Rioux, R. M.; Erdonmez, C. K.; Hughes, S.; Somorjai, G. A.; Alivisatos, A. P. Formation of Hollow Nanocrystals through the Nanoscale Kirkendall Effect. *Science* **2004**, *304*, 711−714.

(16) Wang, W.; Dahl, M.; Yin, Y. Hollow Nanocrystals through the Nanoscale Kirkendall Effect. *Chem. Mater.* **2013**, *25*, 1179−1189.

(17) Fan, H. J.; Gosele, U.; Zacharias, M. Formation of Nanotubes and Hollow Nanoparticles based on Kirkendall and Diffusion Processes: a Review. *Small* **2007**, *3*, 1660−1671.

(18) Shen, L.; Yu, L.; Wu, H. B.; Yu, X. Y.; Zhang, X.; Lou, X. W. Formation of Nickel Cobalt Sulfide Ball-In-Ball Hollow Spheres with Enhanced Electrochemical Pseudocapacitive Properties. *Nat. Commun.* **2015**, *6*, 6694.

(19) Fan, H. J.; Knez, M.; Scholz, R.; Nielsch, K.; Pippel, E.; Hesse, D.; Zacharias, M.; Gosele, U. Monocrystalline Spinel Nanotube Fabrication based on the Kirkendall Effect. *Nat. Mater.* **2006**, *5*, 627−631.

(20) Son, Y.; Son, Y.; Choi, M.; Ko, M.; Chae, S.; Park, N.; Cho, J. Hollow Silicon Nanostructures *via* the Kirkendall Effect. *Nano Lett.* **2015**, *15*, 6914−6918.

(21) Liang, J.; Li, X.; Cheng, Q.; Hou, Z.; Fan, L.; Zhu, Y.; Qian, Y. High Yield Fabrication of Hollow Vesica-Like Silicon based on the Kirkendall Effect and Its Application to Energy Storage. *Nanoscale* **2015**, *7*, 3440−3444.

(22) Liu, B.; Zeng, H. C. Fabrication of ZnO "Dandelions" *via* a Modified Kirkendall Process. *J. Am. Chem. Soc.* **2004**, *126*, 16744−16746.

(23) Choi, S.; Bok, T.; Ryu, J.; Lee, J.-I.; Cho, J.; Park, S. Revisit of Metallothermic Reduction for Macroporous Si: Compromise Between Capacity and Volume Expansion for Practical Li-Ion Battery. *Nano Energy* **2015**, *12*, 161−168.

(24) Bao, Z.; Weatherspoon, M. R.; Shian, S.; Cai, Y.; Graham, P. D.; Allan, S. M.; Ahmad, G.; Dickerson, M. B.; Church, B. C.; Kang, Z.; Abernathy, H. W., III; Summers, C. J.; Liu, M. L.; Sandhage, K. H. Chemical Reduction of Three-Dimensional Silica Micro-Assemblies into Microporous Silicon Replicas. *Nature* **2007**, *446*, 172−175.

(25) Yu, Y.; Gu, L.; Zhu, C. B.; Tsukimoto, S.; Aken, P. A. v.; Maier, J. Reversible Storage of Lithium in Silver-Coated Three-Dimensional Macroporous Silicon. *Adv. Mater.* **2010**, *22*, 2247−2250.

(26) Lin, N.; Han, Y.; Zhou, J.; Zhang, K. L.; Xu, T. J.; Zhu, Y. C.; Qian, Y. T. a Low Temperature Molten Salt Process for Aluminothermic Reduction of Silicon Oxides to Crystalline Si for Li-Ion Batteries. *Energy Environ. Sci.* **2015**, *8*, 3187−3191.

(27) Mishra, K.; Zheng, J.; Patel, R.; Estevez, L.; Jia, H.; Luo, L.; El-Khoury, P. Z.; Li, X.; Zhou, X.-D.; Zhang, J.-G. High Performance Porous Si@C Anodes Synthesized by Low Temperature Aluminothermic Reaction. *Electrochim. Acta* **2018**, *269*, 509−516.

(28) Liu, X.; Giordano, C.; Antonietti, M. a Molten-Salt Route for Synthesis of Si and Ge Nanoparticles: Chemical Reduction of Oxides by Electrons Solvated in Salt Melt. *J. Mater. Chem.* **2012**, *22*, 5454−5459.

(29) Pitzer, K. S. Solubility and the Nature of Bonding in Fused Alkali Halide-Metal Systems. *J. Am. Chem. Soc.* **1962**, *84*, 2025−2028.

(30) Stöber, W.; Fink, A.; Bohn, E. Controlled Growth of Monodisperse Silica Spheres in the Micron Size Range. *J. Colloid Interface Sci.* **1968**, *26*, 62−69.

(31) Yu, X.; Xue, F.; Huang, H.; Liu, C.; Yu, J.; Sun, Y.; Dong, X.; Cao, G.; Jung, Y. Synthesis and Electrochemical Properties of Silicon Nanosheets by DC Arc Discharge for Lithium-Ion Batteries. *Nanoscale* **2014**, *6*, 6860−6865.

(32) Wang, R. P.; Zhou, G. W.; Liu, Y. L.; Pan, S. H.; Zhang, H. Z.; Yu, D. P.; Zhang, Z. Raman Spectral Study of Silicon Nanowires: High-Order Scattering and Phonon Confinement Effects. *Phys. Rev. B: Condens. Matter Mater. Phys.* **2000**, *61*, 16827−16832.

(33) Luo, W.; Wang, X.; Meyers, C.; Wannenmacher, N.; Sirisaksoontorn, W.; Lerner, M. M.; Ji, X. Efficient Fabrication of Nanoporous Si and Si/Ge Enabled by a Heat Scavenger in Magnesiothermic Reactions. *Sci. Rep.* **2013**, *3*, 2222.

(34) Wang, B.; Li, X.; Zhang, X.; Luo, B.; Zhang, Y.; Zhi, L. Contact-Engineered and Void-Involved Silicon/Carbon Nanohybrids as Lithium-Ion-Battery Anodes. *Adv. Mater.* **2013**, *25*, 3560−3565.

(35) Gao, P.; Tang, H.; Xing, A.; Bao, Z. Porous Silicon from the Magnesiothermic Reaction as a High-Performance Anode Material for Lithium Ion Battery Applications. *Electrochim. Acta* **2017**, *228*, 545−552.

(36) Wang, L.; Lin, N.; Zhou, J.; Zhu, Y.; Qian, Y. Silicon Nanoparticles Obtained *via* a Low Temperature Chemical "Metathesis" Synthesis Route and Their Lithium-Ion Battery Properties. *Chem. Commun.* **2015**, *51*, 2345−2348.

(37) Hai, N. H.; Grigoriants, I.; Gedanken, A. Converting Stober Silica and Mediterranean Sand to High Surface Area Silicon by a Reaction under Autogenic Pressure at Elevated Temperatures. *J. Phys. Chem. C* **2009**, *113*, 10521−10526.

DOI: 10.1021/acsnano.8b06528
ACS Nano 2018, 12, 11481−11490

(38) Lu, Z.; Liu, N.; Lee, H. W.; Zhao, J.; Li, W.; Li, Y.; Cui, Y. Nonfilling Carbon Coating of Porous Silicon Micrometer-Sized Particles for High-Performance Lithium Battery Anodes. *ACS Nano* **2015**, *9*, 2540−2547.
(39) Zang, J.; An, T.; Dong, Y.; Fang, X.; Zheng, M.; Dong, Q.; Zheng, N. Hollow-In-Hollow Carbon Spheres with Hollow Foam-Like Cores for Lithium-Sulfur Batteries. *Nano Res.* **2015**, *8*, 2663−2675.
(40) Liu, R.; Mahurin, S. M.; Li, C.; Unocic, R. R.; Idrobo, J. C.; Gao, H.; Pennycook, S. J.; Dai, S. Dopamine as a Carbon Source: the Controlled Synthesis of Hollow Carbon Spheres and Yolk-Structured Carbon Nanocomposites. *Angew. Chem., Int. Ed.* **2011**, *50*, 6799−6802.
(41) Gale, R. J.; Osteryoung, R. A. Investigation of Subvalent Ion Effects During Aluminum. Anodization in Molten NaCl-AlCl. Solvents. *J. Electrochem. Soc.* **1974**, *121*, 983−987.
(42) Magasinski, A.; Dixon, P.; Hertzberg, B.; Kvit, A.; Ayala, J.; Yushin, G. High-Performance Lithium-Ion Anodes Using a Hierarchical Bottom-Up Approach. *Nat. Mater.* **2010**, *9*, 353−358.
(43) Lin, L.; Xu, X.; Chu, C.; Majeed, M. K.; Yang, J. Mesoporous Amorphous Silicon: a Simple Synthesis of a High-Rate and Long-Life Anode Material for Lithium-Ion Batteries. *Angew. Chem., Int. Ed.* **2016**, *55*, 14063−14066.
(44) Li, X. L.; Yan, P. F.; Arey, B. W.; Luo, W.; Ji, X. L.; Wang, C. M.; Liu, J.; Zhang, J. G. a Stable Nanoporous Silicon Anode Prepared by Modified Magnesiothermic Reactions. *Nano Energy* **2016**, *20*, 68−75.
(45) Tao, H. C.; Huang, M.; Fan, L.-Z.; Qu, X. H. Effect of Nitrogen on the Electrochemical Performance of Core−Shell Structured Si/C Nanocomposites as Anode Materials for Li-Ion Batteries. *Electrochim. Acta* **2013**, *89*, 394−399.
(46) Liu, N.; Hu, L.; McDowell, M. T.; Jackson, A.; Cui, Y. Prelithiated Silicon Nanowires as an Anode for Lithium Ion Batteries. *ACS Nano* **2011**, *5*, 6487−6493.
(47) Ryu, J.; Hong, D.; Choi, S.; Park, S. Synthesis of Ultrathin Si Nanosheets from Natural Clays for Lithium-Ion Battery Anodes. *ACS Nano* **2016**, *10*, 2843−2851.
(48) Liu, N.; Lu, Z.; Zhao, J.; McDowell, M. T.; Lee, H. W.; Zhao, W.; Cui, Y. a Pomegranate-Inspired Nanoscale Design for Large-Volume-Change Lithium Battery Anodes. *Nat. Nanotechnol.* **2014**, *9*, 187−192.
(49) Hertzberg, B.; Alexeev, A.; Yushin, G. Deformations in Si-Li Anodes upon Electrochemical Alloying in Nano-Confined Space. *J. Am. Chem. Soc.* **2010**, *132*, 8548−8549.

DOI: 10.1021/acsnano.8b06528
ACS Nano 2018, 12, 11481−11490